## RESEARCH ARTICLE

# 3D THz-TDS SAR Imaging by an Inverse Synthetic Cylindrical Aperture

**DILYAN DAMYANOV, TOBIAS KUBICZEK, KEVIN KOLPATZECK, ANDREAS CZYLWIK, THORSTEN SCHULTZE, AND JAN C. BALZER, (Member, IEEE)**

Faculty of Engineering, Chair of Communication Systems (NTS), University of Duisburg–Essen, 47057 Duisburg, Germany

Corresponding author: Tobias Kubiczek (tobias.kubiczek@uni-due.de)

**ABSTRACT** Terahertz time-domain spectroscopy (THz-TDS) is a promising tool for high-resolution 3D imaging of objects due to the high center frequency and bandwidth compared to microwave systems. In addition, terahertz waves have a higher penetration depth than visible or near-infrared radiation. Typically, optics are used to focus the terahertz radiation onto an object under test. This limits the imaging capability in the axial dimension to the depth of field and limits simple imaging of complex surfaces. In this work, we adapt a backpropagation algorithm from synthetic aperture radar (SAR) imaging to reconstruct high-resolution 3D images from time-domain traces acquired with a lensless THz-TDS system. For this purpose, an inverse cylindrical aperture is used and an equation that describes the maximum achievable resolution as a function of the beam pattern, the bandwidth, and the length of the synthetic aperture is derived. The calculated resolution is 960 $\mu$m for the linear dimension of the aperture and 75 $\mu$m for the rotationally symmetric dimension of the cylindrical aperture for a bandwidth of 2 THz. The resolving power is verified by measurements on metallic and dielectric objects. In the future, this method can be used for non-destructive testing of objects with complex shaped surfaces and internal structures.

**INDEX TERMS** Synthetic aperture radar, terahertz time-domain spectroscopy, lensless terahertz imaging, radar migration algorithms.

## I. INTRODUCTION

Due to the high frequency bandwidth and relatively high penetration depth, imaging in the terahertz frequency range is becoming more and more popular [1], [2], [3]. Applications include security screening [4], [5], medical research [6] and art conservation [7]. Typically, a terahertz image is generated using mirrors and/or lenses to focus the terahertz beam onto the surface of the object under test (OUT). The specular reflections from the surface are captured by a detector. However, to generate a correct and high-resolution image using this method, knowledge about the precise position, orientation, and shape of the OUT is needed [8], [9], [10]. As the spot size of the focused terahertz beam is frequency-dependent, a "perfect" focus for all spectral components is not possible.

The associate editor coordinating the review of this manuscript and approving it for publication was Saroj Tripathi.

Additionally, the minimum achievable spot-size depends on the numerical aperture (NA) of the optical system. All of these drawbacks limit the applications of terahertz imaging in real-life scenarios. Thus, in [11] and [12] we proposed a terahertz time-domain spectroscopy (THz-TDS) based imaging approach using a divergent beam and a synthetic aperture for 2D imaging.

In this paper, we build on our previous work and demonstrate an approach for 3D THz-TDS imaging that overcomes the drawbacks of focused terahertz setups, yet maintains a high resolution in all three dimensions. The approach employs the use of a synthetic cylindrical aperture with a divergent terahertz beam and a post-processing procedure for the digital focusing. Using this method, the lateral resolution of the approach is not limited by the spot size of the focused terahertz beam. Here, the resolution is determined by the properties of the synthetic aperture: the absolute bandwidth,

the center frequency, and the beam divergence. A detailed analysis of these factors is carried out. Finally, the evaluation and validation of the imaging method is carried out with measurements on different metallic and dielectric OUTs using a state-of-the-art THz-TDS system. To the best of our knowledge, this is the first demonstration of 3D image reconstruction with a synthetic cylindrical aperture and THz-TDS. Additionally, the achieved resolution closes the gap between conventional terahertz imaging and near-field imaging. The measurement setup is easy to set up and offers advantages over other methods in terms of complexity.

In section II, an analysis of the parameters that have an impact on the quality of the synthetic aperture is performed. In section III, the properties of the linear, circular, and cylindrical aperture are discussed. In section IV, measurement results on different OUTs are presented for the cylindrical aperture.

## II. MEASUREMENT SYSTEM

The measurement system employed in this work is a commercially available THz-TDS system (TERA K15, Menlo Systems). The setup consists of a femtosecond laser source (C-Fiber with 1560 nm wavelength), a high-resolution computer-controlled 1700 ps long optomechanical delay unit (ODU), a fiber-coupled photoconductive antenna (PCA) as the emitter (TERA 15-TX-FC Fe:InGaAs) and a fiber-coupled PCA as the detector (TERA 15-RX-FC LT InGaAs). The antennas are mounted in a divergent reflection geometry without additional optics. Thus, no collimating or focusing optics are employed and measurements are performed with a divergent beam. In the following, an evaluation of the system specifications is given.

### A. DYNAMIC RANGE AND FREQUENCY BANDWIDTH EVALUATION

To estimate the maximum obtainable frequency bandwidth and dynamic range of the employed measurement system, measurements with a reference object in a reflection geometry are performed. A large metal plate is used as a reference object. This is an optimal reflection scenario compared to the objects that will be measured later. Due to the low emitted energy, the evaluation of the signals is performed using averaged traces.

Fig. 1 shows the measured THz-TDS trace against a metal plate with 60 averages. The time-domain trace in Fig. 1a has a full width at half maximum (FWHM) of $\tau_{\text{FWHM}} = 0.44$ ps. The frequency spectrum in Fig. 1b shows a maximum signal to noise power ratio of about 37 dB and a detectable frequency bandwidth of 2 THz.

### B. PCA CHARACTERIZATION

Another parameter of the measurement setup that contributes to the image reconstruction is the shape of the divergent beam generated by the PCA. As THz-TDS systems are typically used for measurements with a focused or collimated beam, the antenna pattern of the PCA has not yet been investigated
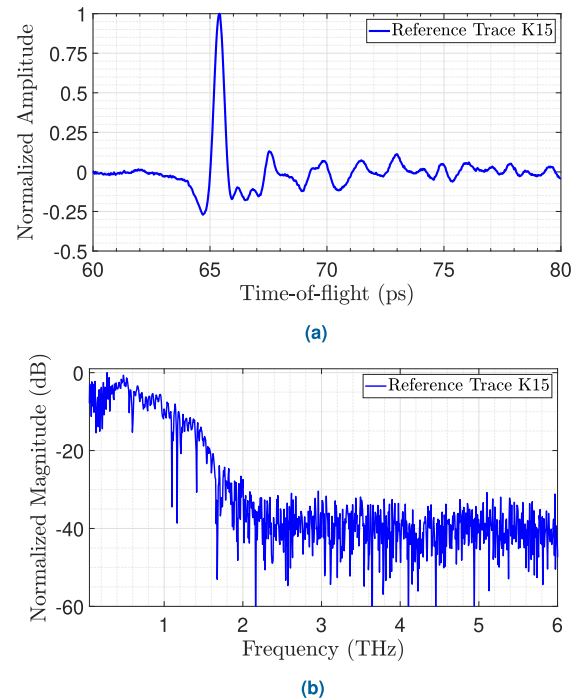


**FIGURE 1.** Averaged reference measurement over 60 single-shot traces in a reflection geometry using a divergent terahertz beam. The time-domain trace is shown in (a) and the corresponding frequency-domain spectrum in (b).
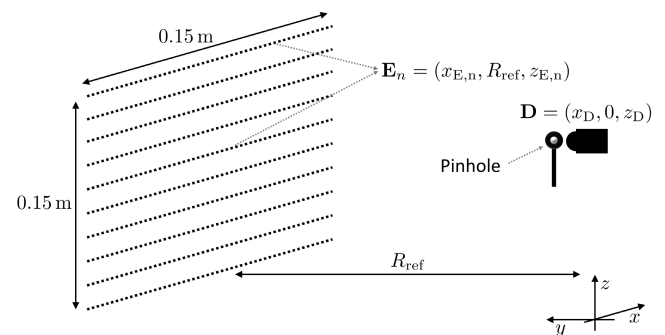


**FIGURE 2.** Measurement setup for the PCA characterization experiment. The detector position **D** is fixed and the emitter at position **E$_n$** is moved in 1 mm steps along the $x$- and $z$- axes as represented by the dotted lines. The range distance between **D** and the dotted plane is $R_{\text{ref}}$.

in detail. To analyze the shape of the beam, the measurement scenario in Fig. 2 is employed.

The two antennas are positioned facing each other at a distance of $R_{\text{ref}} = 140$ mm in the $y$-direction. The detector antenna at position $\mathbf{D} = (x_D, 0, z_D)$ is fixed at this position with $x_D = z_D = 75$ mm. A pinhole is positioned in front of the detector to analyze the pattern of the emitter. The emitter at position $\mathbf{E}_n = (x_{E,n}, R_{\text{ref}}, z_{E,n})$ is moved along the $x$- and $z$-direction in 1 mm steps, represented in the figure by the black dots. At each position, a measurement is performed. The detected signal $s_n(x, R_{\text{ref}}, z, t)$ is averaged over 60 traces. To evaluate the antenna characteristics, the FWHM, the peak magnitude, and the fidelity of the antennas are evaluated.

The fidelity is the maximum correlation between the trace for the case that the antennas are directly in front of each other $s_0(x_D, R_{ref}, z_D, t)$ and traces at different positions. Accordingly to [13] and [14], it is defined as:

$$F_n(x, z) = \max_\tau \int s_0(x_D, R_{ref}, z_D, t) \cdot s_n(x, R_{ref}, z, t - \tau)dt. \tag{1}$$

The fidelity is used in antenna technology to assess the quality and distortion of a detected pulse based on the angle at which the pulse is detected. Hence, a high fidelity equal to one is desirable. The results for the three parameters in polar form are presented in Fig. 3, where $\psi_{az}$ is the azimuth angle (the angle to the $x$-axis) and $\phi_{el}$ is the elevation angle (the angle to the $z$-axis).



**(a)** Peak magnitude
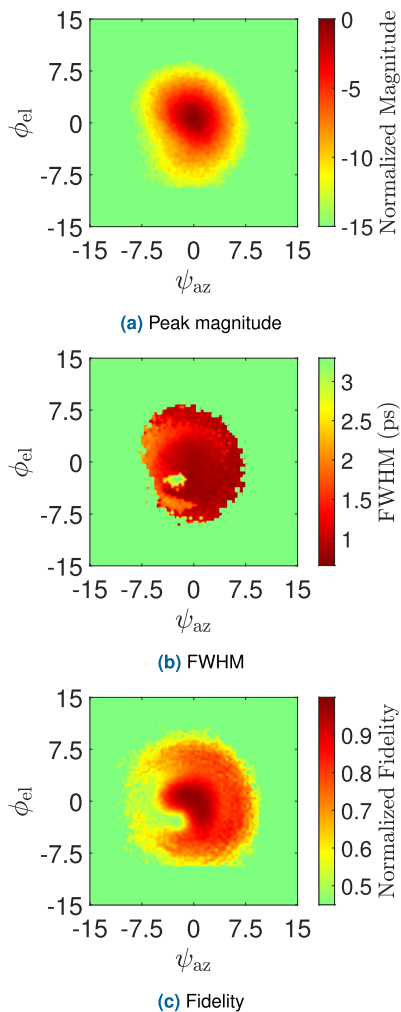


**(b)** FWHM



**(c)** Fidelity

**FIGURE 3.** Results for the peak magnitude (a), the FWHM (b) and the fidelity (c) of the experiment for the characterization of the PCA with respect to the azimuth $\psi_{az}$ and elevation $\phi_{el}$ angles.

The results for the normalized magnitude from Fig. 3a are consistent with a Gaussian-shaped beam with a $-3$ dB beamwidth in elevation $\phi_{el,-3\,dB} = 5.45°$ and azimuth $\psi_{az,-3\,dB} = 5.2°$. The $-15$ dB beamwidth is

approximately the same for azimuth and elevation with $\psi_{az,-15\,dB} \approx \phi_{el,-15\,dB} \approx 18°$. For azimuth and elevation angles in the range $-9° \leq \psi_{az}, \phi_{el} \leq 9°$, the normalized fidelity exhibits values $\geq 0.7$ as can be seen in Fig. 3c. The fidelity drops to 0.55 in the region $\psi_{az} \leq -1.6°$ and $-3° \leq \phi_{el} \leq 3°$. The same is observed for the FWHM in Fig. 3b, as the values for the FWHM in the range $-9° \leq \psi_{az}, \phi_{el} \leq 9°$ are almost constant around 1 ps. However, in the same range where the fidelity drops to 0.55, the FWHM increases by a factor of 2 to 3. This results from a broadening of the terahertz pulse leading to a in higher FWHM and poor fidelity. In conclusion, the PCA generates a narrow Gaussian-shaped beam with a $-3$ dB beamwidth of approx $5°$ in azimuth and elevation direction.

All characteristics for the THz-TDS system are summarized in table 1.

**TABLE 1.** System characteristics for an averaging over 60 THz-TDS traces.

| System Parameter | Value |
|---|---|
| center frequency | 1 THz |
| bandwidth | 2 THz |
| THz-TDS trace FWHM | 0.44 ps |
| signal to noise power ratio | 37 dB |
| PCA beam shape | Gaussian |
| PCA -3 dB beamwidth | |
|   - elevation | 5.45° |
|   - azimuth | 5.25° |
| PCA -15 dB beamwidth | 18° |

## III. IMAGING PRINCIPLE AND RESOLUTION CONSIDERATION FOR 3D TERAHERTZ IMAGING

In our previous work [11], [12], we have demonstrated the principle of 2D THz-TDS imaging using the radar back-projection technique. Here, a brief overview is given as the basis for the 3D imaging technique. In Fig. 4, the
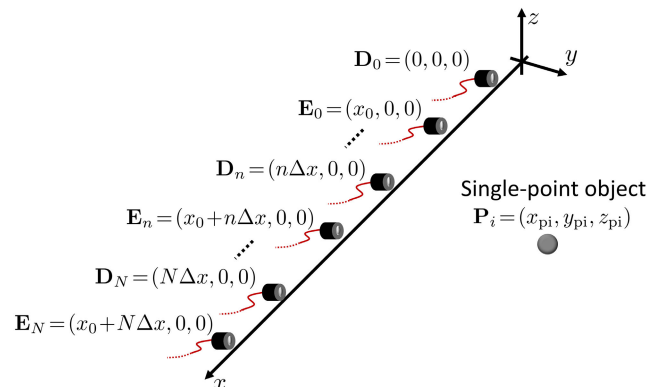


**FIGURE 4.** Measurement model for synthetic aperture imaging. The emitter $E_n$ and detector $D_n$ are linearly moved along the $x$-axis with the step size $\Delta x$. For each position, a measurement of the OUT is performed which is here a single-point object at $P_i$ with $x_{p0} = 0$ mm, $y_{p0} = 150$ mm, and $z_{p0} = 0$ mm.

measurement model for synthetic aperture imaging is presented for the case of a linear synthetic aperture.

In the model, an emitter at position $\mathbf{E}_0$ and a detector at position $\mathbf{D}_0$ are linearly moved along the $x$-axis with the step size $\Delta x$. The distance between the emitter and the detector is kept constant. For each position $n$, a terahertz pulse is transmitted and the detector is measuring the reflected signal from the single-point object at position $\mathbf{P}_i$ with $n = 0 \ldots N$. The detected signal $s_{\mathrm{d}}(\mathbf{E}_n, \mathbf{D}_n, t)$ can be expressed as

$$s_{\mathrm{d}}(\mathbf{E}_n, \mathbf{D}_n, t) = \sum_i r(\mathbf{P}_i, \mathbf{E}_n, \mathbf{D}_n) \cdot s_{\mathrm{e}}(t - t_{i,n}), \quad (2)$$

where $s_{\mathrm{e}}(t)$ is the emitted terahertz signal, $r(\mathbf{P}_i, \mathbf{E}_n, \mathbf{D}_n)$ is the reflection coefficient of the object, and $t_{i,n}$ is the time-of-flight the emitted terahertz pulse needs to travel from the emitter to the object and back to the detector. Assuming a constant propagation velocity at the speed of light $c_0$, the time-of-flight is

$$t_{i,n} = \frac{|\mathbf{P}_i - \mathbf{E}_n| + |\mathbf{P}_i - \mathbf{D}_n|}{c_0}. \quad (3)$$

To reconstruct the shape and position of the object, an integration over the synthetic aperture is performed. In the case of a discrete aperture, the integration is substituted by a summation operation and the resulting image $\mathbf{I}(x, y)$ is reconstructed according to

$$\mathbf{I}(x_u, y_v) = \sum_n s_{\mathrm{d}}(\mathbf{E}_n, \mathbf{D}_n, t - t_{u,v,n}), \quad (4)$$

where $t_{u,v,n}$ is the time-of-flight of the terahertz signal to and from an assumed point object at position $\mathbf{P}_{u,v} = (x_u, y_v, 0)$. Using this technique, high-resolution 2D terahertz images can be generated with a divergent beam, where the resolution of the images is a function of the system parameters bandwidth, center frequency, and the geometry of the synthetic aperture. To extend the method for 3D image generation, the synthetic aperture has to be expanded in the $z$-axis, which increases the size and complexity of the aperture geometry. In this paper, we propose an approach for 3D terahertz imaging, where the synthetic aperture is extended by combining multiple circular scans in the $x$-$y$-plane at different $z$-coordinates. This results in a linear synthetic aperture in $z$ and a circular synthetic aperture in $x$ and $y$. In the 3D space, the synthetic aperture is represented by a cylindrical shape. To analyze the resolution limits of the employed synthetic aperture, the two basic geometries are analyzed in detail.

## A. LINEAR SYNTHETIC APERTURE

Based on the movement of the antennas, there are different possible geometries for a synthetic aperture. The most popular geometry is the linear aperture [15], [16], [17], [18]. The emitter-detector pair is moved linearly along the cross-range, which is perpendicular to the propagation direction of the radiation. The propagation direction is also called range direction. Fig. 4 demonstrates the used principle, where the $x$-axis is the cross-range and the $y$-axis is the range dimension.

Based on this geometry, the range $\delta_{\mathrm{r}}$ and cross-range $\delta_{\mathrm{cr}}$ resolution for synthetic aperture imaging systems are defined as [18], [19], and [20]:

$$\delta_{\mathrm{r}} \geq \frac{c_0}{2B}, \quad (5)$$

and

$$\delta_{\mathrm{cr}} \geq \frac{R\lambda_{\mathrm{c}}}{2L_{\mathrm{sa}}}. \quad (6)$$

respectively. $B$ is the frequency bandwidth of the system, $R$ is the distance to the object, $\lambda_{\mathrm{c}}$ is the center wavelength of the emitted signal, and $L_{\mathrm{sa}} = N \cdot \Delta x$ is the length of the synthetic aperture. $N$ is the number of measurements and $\Delta x$ is the distance between two measurement points.

These equations show that the best achievable range resolution for a best-case OUT and ideal sampled synthetic aperture is only limited by the bandwidth of the system, which can be on the order of a couple of THz for commercially available THz-TDS systems. Furthermore, for a fixed range $R$, the cross-range resolution is only limited by the synthetic aperture and the center wavelength. However, the size of the synthetic aperture is limited by the $-3$ dB beamwidth of the PCA. This limits the length of the maximum synthetic aperture $L_{\mathrm{sa,max}}$, since an object can be observed only from a limited angle-of-view with

$$\tan(\psi_{\mathrm{az,-3\,dB}}) = \frac{L_{\mathrm{sa,max}}}{2R}. \quad (7)$$

Substituting $L_{\mathrm{sa,max}}$ for $L_{\mathrm{sa}}$ in (6), the maximum cross-range resolution using the presented system is then

$$\delta_{\mathrm{cr}} \geq \frac{R\lambda_{\mathrm{c}}}{2L_{\mathrm{sa,max}}} = \frac{R\lambda_{\mathrm{c}}}{2 \cdot 2R\tan(\psi_{\mathrm{az,-3\,dB}})} = \frac{\lambda_{\mathrm{c}}}{4\tan(\psi_{\mathrm{az,-3\,dB}})}. \quad (8)$$

Using this equation with $\psi_{\mathrm{az,-3\,dB}} = 5°$, the cross-range resolution is given as

$$\delta_{\mathrm{cr}} \geq 2.86 \cdot \lambda_{\mathrm{c}}. \quad (9)$$

In the following, the result of a simulation for a single-point object is presented using the parameters of the antennas acquired from the experiment described in section II-B, the system parameters from section II-A, and equation (4). The reflection coefficient $r(\mathbf{P}_i, \mathbf{E}_n, \mathbf{D}_n) = 1$ is weighted with the azimuth beam profile of the PCA antenna. The resulting image of a single-point object is shown in Fig. 5.

The result of the simulation shows a cross-range resolution of $960\,\mu\mathrm{m}$ which is comparable to the optimum resolution with the given parameters from (9) of $\delta_{\mathrm{cr}} = 860\,\mu\mathrm{m}$. Additionally, the Gaussian beam profile of the PCA antennas further decreases the cross-range resolution as the bistatic measurement scenario has a strong angular selectivity for close objects. A further quality indicator for the PSF is the peak side lobe ratio (PSLR) which is $-17.38$ dB.
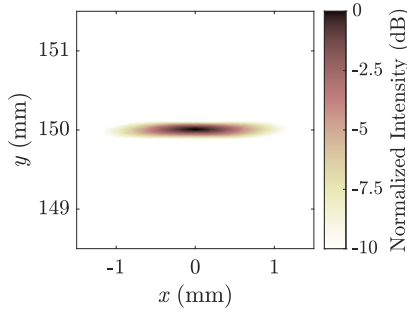
**FIGURE 5.** Reconstructed image of a simulated single-point object for the measured PCA pattern.

## B. CIRCULAR SYNTHETIC APERTURE

The second type of geometry used for 3D terahertz imaging presented here is the circular synthetic aperture. The OUT is placed in the center of a rotating aperture and is illuminated from all angles as shown in Fig. 6.
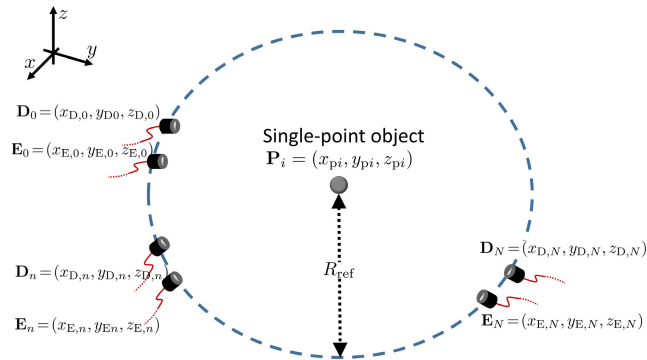


**FIGURE 6.** Measurement setup for a circular synthetic aperture. The emitter-detector pair at positions $\mathbf{E}_n$ and $\mathbf{D}_n$, respectively, are moved along a circle with radius $R_{\text{ref}}$ from the single-point object at position $\mathbf{P}_i$.

The emitter-detector pair is rotated on a circle with the radius $R_{\text{ref}}$ with the propagation direction pointing to the center of the circle. This results in a circular synthetic aperture, where no range and cross-range resolution can be defined. Instead, the $x$ and $y$ resolution components $\delta_x$ and $\delta_y$ are used. This geometry has been applied for narrowband and broadband radar systems with rectangular-shaped frequency spectra with $B_{\text{fr}} < 1$, where $B_{\text{fr}} = B/f_c$ is the fractional bandwidth, and $f_c$ is the center frequency. This results in an increased resolution capability compared to a linear synthetic aperture [21], [22], [23], [24], [25], [26]. By using a complete 360° scan, the resolution in $x$- and $y$-direction is identical [21], [22]:

$$\delta_x = \delta_y = \frac{2.4}{\frac{2\pi f_c}{c_0}} = \frac{2.4 \lambda_c}{2\pi}. \tag{10}$$
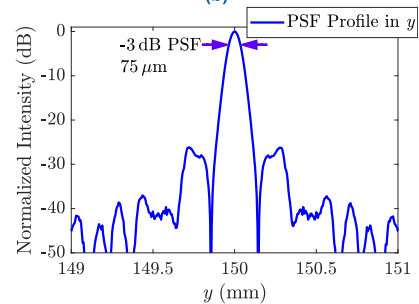
Comparing (9) and (5) as the $x$- and $y$-resolution components of the linear synthetic aperture, to (10) for the $x$- and $y$-resolution of the circular synthetic aperture shows an improvement of the theoretical limit in $x$-direction by a
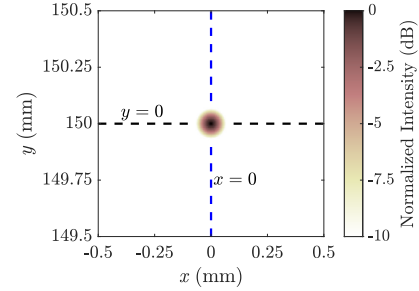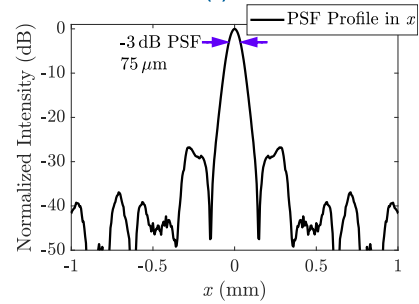


**FIGURE 7.** Simulated PSF of a THz-TDS imaging setup using a circular synthetic aperture. In (a) the shape of the PSF in the $x$-$y$-plane is demonstrated while (b) and (c) show the profile of the PSF for $y = 150\,\text{mm}$ and $x = 0\,\text{mm}$, respectively.

factor of $1.2/2\pi \approx 0.19$. To derive the resolution in the $y$-dimension, we substitute $B = 2 \cdot f_c$ in (5), as the THz-TDS bandwidth is approximately twice the center frequency. Equation (10) shows a resolution in $y$ of $\delta_y \approx 1.5 \cdot \delta_r$. However, (10) is derived for radar systems with $B_{\text{fr}} < 1$ and not for wideband systems such as THz-TDS systems.

To evaluate the effects of the bandwidth on the resolution, a simulation is performed using a single-point object at position $\mathbf{P}_i$ positioned at the center of the circular aperture. The frequency bandwidth of the system is chosen to be $B = 2\,\text{THz}$. With the center of rotation being at $x = 0\,\text{mm}$ and $y = 150\,\text{mm}$, the radius of rotation is $R_{\text{ref}} = 150\,\text{mm}$. As the single-point object is at the center of rotation, it is illuminated at a 90° angle of incidence and hence $r(\mathbf{P}_i, \mathbf{E}_n, \mathbf{D}_n) = 1$ is considered for all positions $\mathbf{E}_n$ and $\mathbf{D}_n$. The angular range of the synthetic aperture is defined by $\theta_{\text{sa}}$, with $\theta_{\text{sa}} = N \cdot \Delta\theta_{\text{sa}}$, where $N$ is the number of measurements and $\Delta\theta_{\text{sa}}$ is the angular step size of the circular aperture.

The result of a simulation with $\theta_{\text{sa}} = 360°$ and $\Delta\theta_{\text{sa}} = 1°$ is shown in Fig. 7. The single-point object is correctly

reconstructed. The intensity profile of the reconstructed objects exhibits an approximately Gaussian shape with $\delta_x = \delta_y$. To further analyze the shape of the point spread function (PSF) in the $x$- and $y$-dimensions and the 3 dB resolution of the image, the reconstructed image in Fig. 7a is sliced along the $x$- and $y$-axis for $y = 150\,\text{mm}$ and $x = 0\,\text{mm}$, respectively. The results are shown in Fig. 7b and Fig. 7c. Here, an approximately Gaussian shape of the PSF in both dimensions can be seen and the 3 dB resolution is identical and equal to $\delta_x = \delta_y \approx 75\,\mu\text{m} = c_0/2B$ with a PSLR of $-26.77$ dB.

Compared to the results of the simulation with a linear synthetic aperture, this shows an improvement factor in the resolution in $x$-direction of 0.282 while maintaining the high resolution in $y$-direction. These results demonstrate the higher resolution capabilities of the employed circular synthetic aperture THz-TDS imaging setup compared to a linear synthetic aperture and radar-based circular synthetic aperture imaging methods with a lower bandwidth.

To further analyze the limits of the circular synthetic aperture, a limited synthetic aperture is considered. This simulates practical scenarios where only a restricted aperture is possible due to obstacles or shadowing effects from different objects or different geometrical features of the considered object. Thus, a set of simulations is performed for different values of $\theta_{\text{sa}}$ to evaluate the effect of the size of the synthetic aperture. The simulation scenario is presented in Fig. 8.
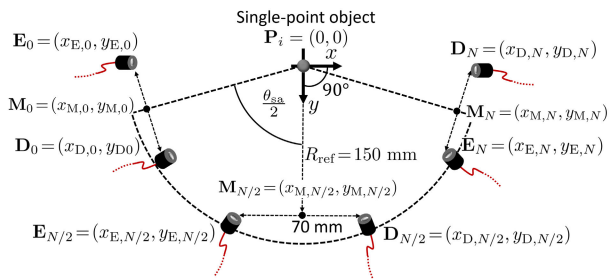


**FIGURE 8.** Measurement model for a partial circular synthetic aperture with $\theta_{\text{sa}}$ representing the angles used for the generation of the synthetic aperture. The single-point object is located at the center of the partial circle and measurements with the emitter at position $\mathbf{E}_n$ and the detector at position $\mathbf{D}_n$, are performed at a radius $R_{\text{ref}}$. $\mathbf{M}_n$ represents the middle point between $\mathbf{E}_n$ and $\mathbf{D}_n$.

The single-point object is positioned at the center of rotation of the partial circular synthetic aperture, i.e. at the origin of the coordinate system. The distance between the emitter positions $\mathbf{E}_n$ and the detector positions $\mathbf{D}_n$ is 70 mm. $\mathbf{M}_n$ is the middle point between $\mathbf{E}_n$ and $\mathbf{D}_n$. The step size of the synthetic aperture is $\Delta\theta_{\text{sa}} = 1°$. For $n = N/2$, $\mathbf{M}_n$ forms a 90° angle with the $x$-axis as shown in Fig. 8. Thus, the synthetic aperture is symmetric with respect to the $y$-axis. The distance from $\mathbf{M}_n$ to the center of rotation is $R_{\text{ref}} = 150\,\text{mm}$. For the simulation, values for $\theta_{\text{sa}}$ in the range from 4° to 360° are considered. In Fig. 9, the reconstructed images of the single-point object for $\theta_{\text{sa}}$ equal to 20°, 60°, 90°, 120°, and 180° are shown.
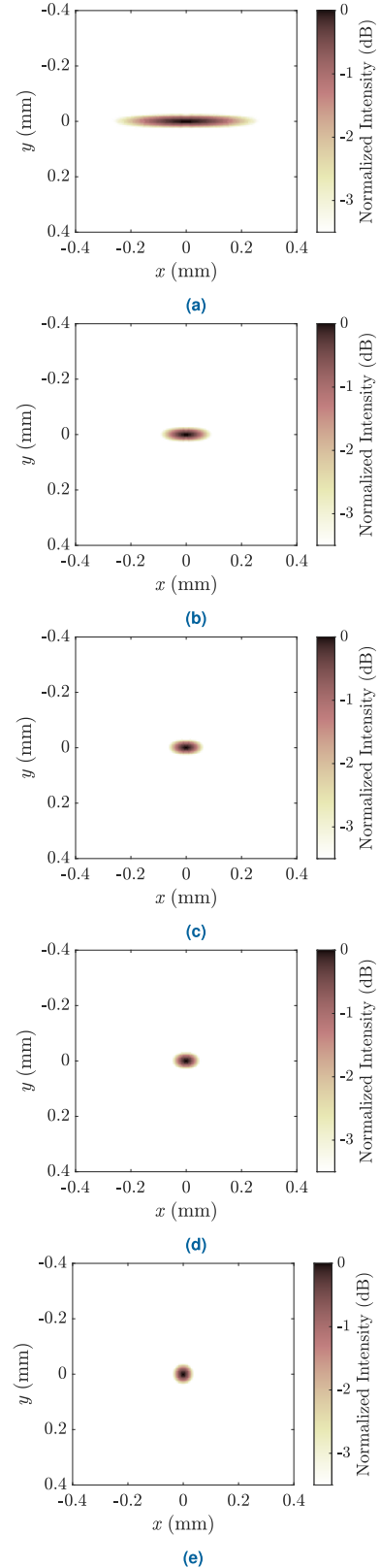


**FIGURE 9.** Resulting PSF for a restricted circular synthetic aperture with $\theta_{\text{sa}}$ equal to 20° (a), 60° (b), 90° (c), 120° (d), and 180° (e).

The reconstructed images show that the resolution in the $y$ - direction remains constant with $\delta_y = c_0/2B$ for all values

of $\theta_{sa}$ if the synthetic aperture is symmetrical to the $y$-axis. The resolution in the $x$-direction improves with increasing $\theta_{sa}$ for $\theta_{sa} < 180°$. Furthermore, for $\theta_{sa} > 180°$ the resolution in the $x$-direction reaches the resolution for a complete circular aperture of $\delta_x = c_0/2B$. Using the results from the simulations, an approximation for the image resolution is given as

$$\delta_x \approx \begin{cases} \dfrac{c_0}{2B} \cdot \dfrac{180°}{\theta_{sa}}, & \text{for } 0° < \theta_{sa} < 180° \\[2mm] \dfrac{c_0}{2B}, & \text{for } \theta_{sa} \geq 180° \end{cases} \quad (11)$$

and

$$\delta_y = \frac{c_0}{2B}. \quad (12)$$

In Fig. 10 the image resolution in $x$-direction as a function of the synthetic apertures calculated with (11) is compared to the $-3$ dB width of the PSF extracted from the simulated images. The results show a good agreement between the simplified equation for the resolution and the simulation results.
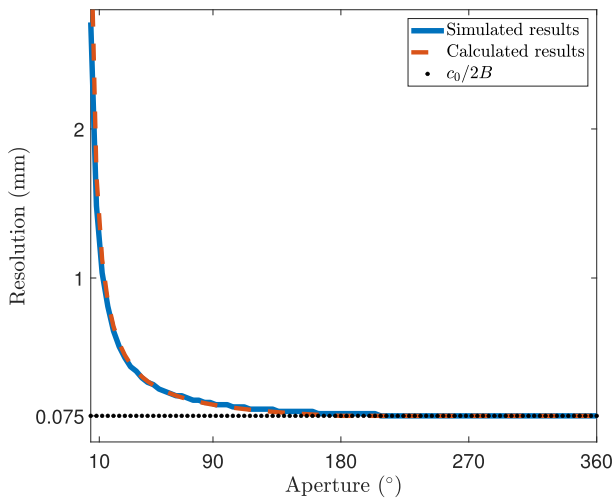
**FIGURE 10.** Simulated (blue) and calculated (red) according to equation (11) $-3$ dB width of the PSF in $x$ for a THz-TDS imaging system with a circular synthetic aperture. The theoretical limit of $c_0/2B$ is shown as the black dotted line.

## C. CYLINDRICAL SYNTHETIC APERTURE FOR 3D THz IMAGES

As mentioned above, the synthetic aperture has to be extended in all three dimensions to generate 3D images. In the method proposed in this paper, the two geometries are now combined to a cylindrical synthetic aperture as shown in Fig. 11.

The cylindrical synthetic aperture consists of a linear synthetic aperture along the $z$-axis and a circular synthetic aperture in the $x$- and $y$-dimensions. The OUT is positioned on a rotation stage which simulates a rotation of the emitter and detector positions $\mathbf{E}_n$ and $\mathbf{D}_n$ around the object in the $x$-$y$-plane. The distance to the object is defined as $R_{ref}$ and the circular synthetic aperture is specified by the angle $\theta_{sa}$. The rotation stage is positioned on a linear translation stage which
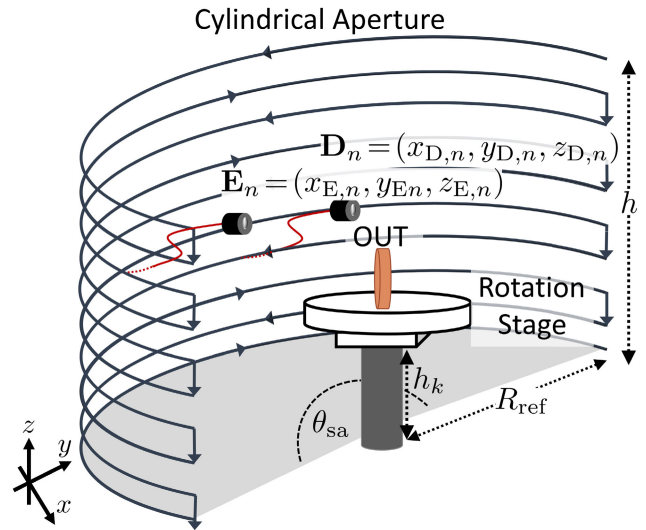
**FIGURE 11.** Measurement setup for a 3D cylindrical synthetic aperture. An OUT is positioned on a rotation stage and a linear moving platform in the $z$-direction that simulates the movement of the detector and emitter at positions $\mathbf{D}_n$ $\mathbf{E}_n$. The rotational stage rotates from $0°$ to $\theta_{sa}$ resulting in a partial cylindrical synthetic aperture.

is moved with steps of $\Delta h$ along the $z$-axis. For each position $h_k$, a new measurement using the circular synthetic aperture is performed. Thus, a cylindrical synthetic aperture is achieved. The height of the cylindrical synthetic aperture is given as $h_{sa}$. Using this measurement scenario, the shape and size of the OUT in all three dimensions can be reconstructed, where the resolution along the $z$-axis corresponds to the resolution of a linear synthetic aperture according to (9) and the resolution along the $x$- and $y$-axis is calculated using (11) and (12), respectively.
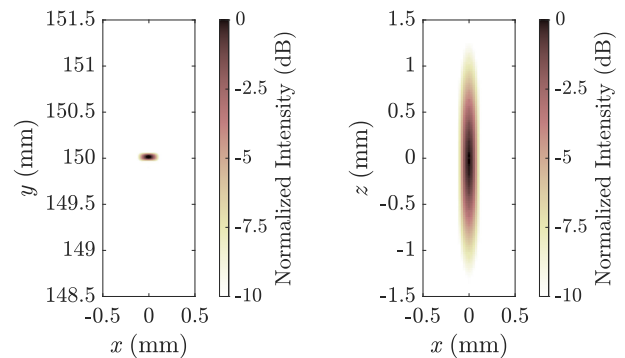
**FIGURE 12.** Resulting PSF of the 3D imaging setup in the $x$-$y$- (left) and $x$-$z$- (right) planes.

In Fig. 12, slices along the $z$- and $y$-axis of a three dimensional PSF for a single-point object located at $(0, 150, 0)$ mm with $h_{sa} = 26.2$ mm, $R_{ref} = 150$ mm, and $\theta_{sa} = 90°$ are shown. The 2D shape of the PSF in the $x$-$y$-plane in Fig. 12 results from the circular synthetic aperture of the cylindrical geometry and is comparable to the result shown in Fig. 9c. The resolution in $x$-direction is $150\,\mu$m and the resolution in $y$-direction is $75\,\mu$m. On the right side of Fig. 12, the shape

of the sliced PSF in the $x$-$z$-plane is shown. The resolution in $z$-direction is $960\,\mu$m. The PSF exhibits the same shape as the PSF in Fig. 5 and contributes to the resolution of the system in the $x$-$z$-plane. Due to the higher resolution capabilities of the circular aperture, the reconstructed images using the presented approach have a higher resolution in the $x$-$y$-plane than in the $x$-$z$-plane. The PSLR is $-26.6\,$dB in both directions.

## IV. EXPERIMENTAL RESULTS FOR 3D IMAGING

The experimental results for 3D terahertz imaging in this paper are organized as follows. First, measurements using a resolution test chart are presented. Next, imaging using a common day object, here a 1 euro cent coin, is performed. The coin is placed as a hidden object inside a paper envelope. Finally, a small dielectric object is used as to test the method for dielectric objects.

### A. RESOLUTION RESULTS USING TEST CHART

The first OUT is a resolution test chart as shown in Fig. 13a. The test chart is a printed circuit board (PCB) with the dimensions $121\,$mm $\times$ $121\,$mm, where the black stripes are metal. The distance between the metal stripes is equal to the width of the stripes. The features of interest are with dimensions $\leq 1\,$mm, as shown in Fig. 13a) making them suitable to test the imaging resolution of the system. The parameters used for the cylindrical synthetic aperture are $h = 50\,$mm, $R_{\mathrm{ref}} = 150\,$mm, and $\theta_{\mathrm{sa}} = 160°$. The step size in the $z$ - direction is $\Delta h = 0.4\,$mm and $\Delta\theta_{\mathrm{sa}} = 0.5°$ for the rotation. The test chart is positioned parallel to the $x$-$z$-plane. Thus, all metal stripes have the same $y = y_0$ coordinate. The reconstructed image in the $x$-$z$-plane for $y = y_0$ is shown in Fig. 13b).

The reconstructed image in Fig. 13c) shows a maximum error in the dimensions of the stripes of less than $20\,\mu$m. The results show that the metal stripes are correctly reconstructed with a higher resolution in the $x$-direction than in the $z$-direction. This is in agreement with the theoretical considerations in the previous section. The horizontal stripes in the case of $820\,\mu$m and $1.08\,$mm are clearly reconstructed. The smallest horizontal stripes with a width of $560\,\mu$m are blurred. Their size is well below the resolution limit of the system in the $z$-dimension, which is $\approx 800\,\mu$m according to (9). The difference in the resolution in $x$-direction compared to $z$-direction can be seen in Fig. 13c and Fig. 13d. These two images show single slices of the reconstructed volume along the $z$-axis in Fig. 13c and along the $x$-axis in Fig. 13d. In Fig. 13c, the value $z = 27.1\,$mm is chosen, as here the vertical stripes have widths of $560\,\mu$m and $820\,\mu$m. The width and shape of the stripes are clearly reconstructed. Furthermore, the high resolution of the method in $y$-dimension is demonstrated by comparing the $y$-coordinates of the metal stripes with the base of the resolution chart. The two components are resolved with $40\,\mu$m in the $y$-dimension while exhibiting an intensity difference of $10\,$dB. This is not the case when Fig. 13d is considered. Here, the slice along the $x$-
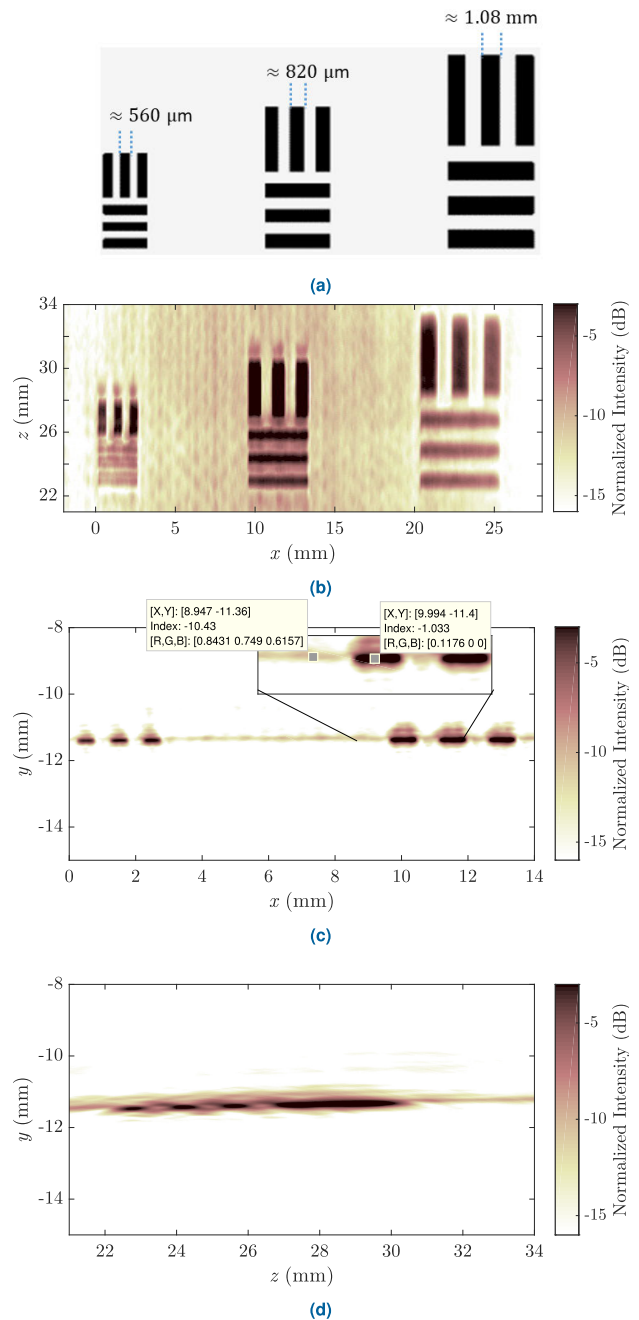


FIGURE 13. A sketch of the test chart (a). The reconstructed test chart (b). Figure (c) shows a slice along the $z$-axis with $z = 27.1\,$mm. Figure (d) shows a slice along the $x$-axis with $x = 11.6\,$mm. The figures demonstrate the higher resolution capabilities of the method in the $x$- and $y$- compared to the $z$-dimension.

axis at $x = 11.6\,$mm shows the reconstructed three horizontal stripes and a single vertical stripe for the $820\,\mu$m stripes.

### B. EXPERIMENTAL RESULTS WITH A COMMON DAY OBJECT

The next OUT is a common day object. We used a 1 euro cent coin, as the dimensions of the coin are well defined

for future comparison purposes. Both sides of the coin were measured simultaneously by using two coins. The two coins are positioned inside an envelope preventing a direct line-of-sight and the envelope is glued to a metal post that is centered at the center of rotation of the cylindrical synthetic aperture. The synthetic aperture has the dimensions of $h = 47$ mm, $R_{\text{ref}} = 120$ mm, and $\theta_{\text{sa}} = 80°$. The step size in the $z$-direction is $\Delta h = 0.4$ mm and the angular step size is $\Delta\theta_{\text{sa}} = 0.4°$. Using the given parameters, the detected terahertz signals are evaluated using the here presented back-propagation. The reconstructed 3D image of the two coins is shown in Fig. 14.
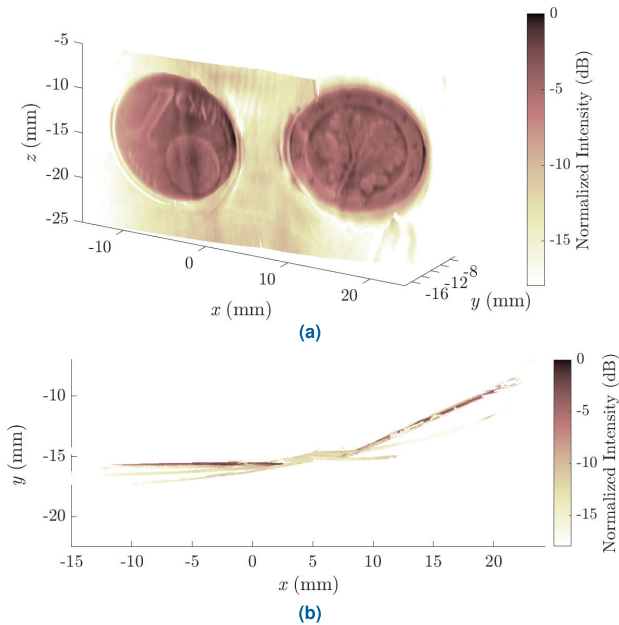




**FIGURE 14.** Reconstructed image of the two 1 euro cent coins inside a paper envelope. In (a) the three dimensional image is shown. The two coins are correctly reconstructed and a part of the envelope is also reconstructed in the image. Figure (b) shows a 2D projection of the volume in the *x*-*y*-plane demonstrating the different orientations and position of the two coins and the envelope in the *x*-*y*-plane.

In Fig. 14a, the reconstructed details of the two coins are clearly visible. On the front side of the coin, the number "1" of the coin together with the text "Cent" are correctly reconstructed. Furthermore, the globe, the diagonal lines, and the stars at the end of the diagonal lines are visible. However, the details on the globe are blurred and the text "Euro" above the "Cent" label is not visible in the image. As for the back side of the coin on the right side of Fig. 14a, the leaf and the stars of the coin are correctly reconstructed. However, the text at the beginning of the leaf, where the minting year and country of origin are printed, is blurred and not readable. In the figure, also a part of the reconstructed envelope can be seen.

In Fig. 14b, an *x*-*y*-view of the reconstructed volume is shown. Here, the different orientation and location of the two reconstructed coins are visible. This result demonstrates not only the high-resolution capabilities of the used terahertz
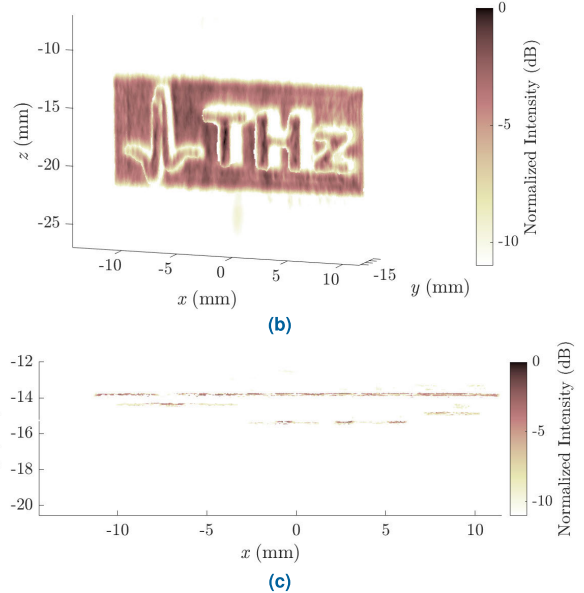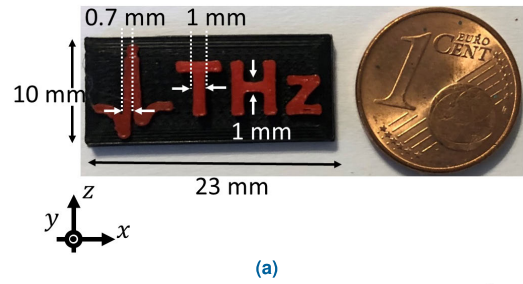


**FIGURE 15.** Reconstructed image and photograph of the test object. In (a) the photograph of the OUT is shown next to a 1 euro cent coin. In (b) the reconstructed three dimensional image is shown. The letters of the THz text and the symbol of the THz-TDS pulse are correctly reconstructed. (c) shows a 2D projection of the volume in the *x*-*y*-plane demonstrating the different depth and range profiles of the symbols.

imaging system, but also the robustness of the setup, as hidden objects with different orientation and location are correctly reconstructed without any *a priori* information despite the antenna position.

**C. EXPERIMENTAL RESULTS WITH A DIELECTRIC OBJECT**
Until now, all measurements were performed with metallic objects with a high reflectivity. However, in many applications objects made of dielectric materials are of interest. Thus, a dielectric object made from a polymer is used for the last experiment. As the OUT, the letters "THz" and the shape of a typical THz-TDS pulse are 3D printed. Fig. 15a shows a photograph of the object next to a 1 euro cent coin. The test object is printed from tough polylactic acid (PLA). The symbols exhibit different heights resulting in different range dimensions in *y* as follows: "T" and "H" have a height of 1.5 mm, "z" of 1 mm, and the pulse symbol of 0.5 mm. The synthetic aperture has the height $h_{\text{sa}} = 45$ mm, the radius $R_{\text{ref}} = 125$ mm, and the angular range $\theta_{\text{sa}} = 180°$. The step size in *z*-direction is $\Delta h = 0.5$ mm and the angular step size is $\Delta\theta_{\text{sa}} = 0.5°$. The object is mounted so that the text and the pulse symbol are in the *x*-*z* plane. The results of the image

reconstruction are shown in Fig. 15, where in Fig. 15b the reconstructed volume in *xyz* is shown and in Fig. 15c the *x* - *y*-projection is shown. The shape and size of the text and the pulse symbol are reconstructed correctly up to the smallest details.

Even the separation between the rising and falling edge of the terahertz pulse symbol is evident. Furthermore, as can be seen in Fig. 15c, the different range profiles of the symbols are reconstructed. The background of the symbols is reconstructed at a range of about 14 mm from the center of rotation. This is consistent with the measurement scenario, as the object is mounted on a metal post positioned at the center of rotation with a radius of 12.5 mm using 1 mm thick double-sided tape.

Closest to the background of the object is the reconstructed THz-TDS pulse form. The mean "height" of the reconstructed pulse is about 520 $\mu$m. A mean error of only 20 $\mu$m is measured. Similar values for the errors are measured for the reconstructed text. For the letters "T" and "H," a mean "height" of 1.51 mm is reconstructed, whereas for the "z" letter the mean "height" is 1.01 mm. This indicates mean errors of just 10 $\mu$m which are on the order of the accuracy of the 3D printer.
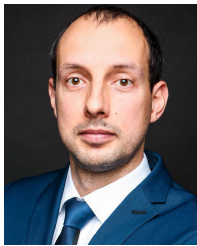
## V. CONCLUSION

In this work, we have presented an approach for broadband terahertz 3D imaging. The measurement setup uses a state-of-the-art THz-TDS system and photoconductive antennas with a divergent beam. The 3dB-beamwidth of the antennas was determined to be 5°. The imaging itself is performed using a synthetic aperture method. Here, we used a cylindrical aperture consisting of a linear and a rotationally symmetric dimension. For both cases, an equation for the resolution was presented based on system parameters such as the size of the synthetic aperture and the frequency bandwidth. The linear dimension gives a resolution of 960 $\mu$m, which is limited by the divergence of the beam. The rotationally symmetric dimension has a resolution limit of 75 $\mu$m, which is comparable to the range (axial) resolution and is limited only by the angle at which the object is observed and the available bandwidth. In addition, we imaged three different objects: a resolution test card, a 1 euro cent coin in an envelope, and a dielectric 3D printed object with letters and a symbol at different heights. All objects were successfully reconstructed. The advantage of the rotational aperture over the linear aperture was clearly demonstrated. In the future, we will extend our method to a spherical synthetic aperture. In this way, 3D imaging with a resolution of less than 100 $\mu$m in all three dimensions will be possible. This will reduce the resolution gap between conventional imaging based on focusing optics and terahertz near-field microscopy. Furthermore, the method can be combined with terahertz ellipsometry to determine reference-free material parameters from the images [27]. Additionally, the use of neural networks could enable a classification of the measured material [28].

## REFERENCES

[1] E. Castro-Camus, M. Koch, and D. M. Mittleman, "Recent advances in terahertz imaging: 1999 to 2021," *Appl. Phys. B, Lasers Opt.*, vol. 128, no. 1, pp. 1–10, Jan. 2022, doi: 10.1007/s00340-021-07732-4.
[2] D. M. Mittleman, "Twenty years of terahertz imaging," *Opt. Exp.*, vol. 26, no. 8, pp. 9417–9431, Apr. 2018.
[3] A. Batra, J. Barowski, D. Damyanov, M. Wiemeler, I. Rolfes, T. Schultze, J. C. Balzer, D. Göhringer, and T. Kaiser, "Short-range SAR imaging from GHz to THz waves," *IEEE J. Microw.*, vol. 1, no. 2, pp. 574–585, Apr. 2021, doi: 10.1109/JMW.2021.3063343.
[4] J. Gao, Z. Cui, B. Cheng, Y. Qin, X. Deng, B. Deng, X. Li, and H. Wang, "Fast three-dimensional image reconstruction of a standoff screening system in the terahertz regime," *IEEE Trans. THz Sci. Technol.*, vol. 8, no. 1, pp. 38–51, Jan. 2018.
[5] K. Humphreys, "Medical applications of terahertz imaging: A review of current technology and potential applications in biomedical engineering," in *Proc. 26th Annu. Int. Conf. IEEE Eng. Med. Biol. Soc.*, San Francisco, CA, USA, Sep. 2004, pp. 1302–1305.
[6] S. Nakajima, H. Hoshina, M. Yamashita, C. Otani, and N. Miyoshi, "Terahertz imaging diagnostics of cancer tissues with a chemometrics technique," *Appl. Phys. Lett.*, vol. 90, no. 4, Jan. 2007, Art. no. 041102.
[7] K. Krugener, M. Schwerdtfeger, S. F. Busch, A. Soltani, E. Castro-Camus, M. Koch, and W. Viöl, "Terahertz meets sculptural and architectural art: Evaluation and conservation of stone objects with T-ray technology," *Sci. Rep.* vol. 5, no. 1, pp. 1–7, 2015.
[8] E. Stübling, Y. Bauckhage, E. Jelli, B. Fischer, B. Globisch, M. Schell, A. Heinrich, J. C. Balzer, and M. Koch, "A THz tomography system for arbitrarily shaped samples," *J. Infr., Millim., THz Waves*, vol. 38, no. 10, pp. 1179–1182, Oct. 2017.
[9] Z. Song, S. Yan, Z. Zang, Y. Fu, D. Wei, H.-L. Cui, and P. Lai, "Temporal and spatial variability of water status in plant leaves by terahertz imaging," *IEEE Trans. THz Sci. Technol.*, vol. 8, no. 5, pp. 520–527, Sep. 2018.
[10] E.-M. Stubling, A. Rehn, T. Siebrecht, Y. Bauckhage, L. Öhrström, P. Eppenberger, J. C. Balzer, F. Ruhli, and M. Koch, "Application of a robotic THz imaging system for sub-surface analysis of ancient human remains," *Sci. Rep.*, vol. 9, no. 1, pp. 1–8, Mar. 2019.
[11] D. Damyanov, B. Friederich, M. Yahyapour, N. Vieweg, A. Deninger, K. Kolpatzeck, X. Liu, A. Czylwik, T. Schultze, I. Willms, and J. C. Balzer, "High resolution lensless terahertz imaging and ranging," *IEEE Access*, vol. 7, pp. 147704–147712, 2019, doi: 10.1109/ACCESS.2019.2934582.
[12] S. Mansourzadeh, D. Damyanov, T. Vogel, F. Wulf, R. B. Kohlhaas, B. Globisch, T. Schultze, M. Hoffmann, J. C. Balzer, and C. J. Saraceno, "High-power lensless THz imaging of hidden objects," *IEEE Access*, vol. 9, pp. 6268–6276, 2021, doi: 10.1109/ACCESS.2020.3048781.
[13] D. Lamensdorf and L. Susman, "Baseband-pulse-antenna techniques," *IEEE Antennas Propag. Mag.*, vol. 36, no. 1, pp. 20–30, Feb. 1994.
[14] Z. N. Chen, X. H. Wu, H. F. Li, N. Yang, and M. Y. W. Chia, "Considerations for source pulses and antennas in UWB radio systems," *IEEE Trans. Antennas Propag.*, vol. 52, no. 7, pp. 1739–1748, Jul. 2004, doi: 10.1109/TAP.2004.831405.
[15] L. J. Cutrona, W. E. Vivian, E. N. Leith, and G. O. Hall, "A high-resolution radar combat-surveillance system," *IRE Trans. Mil. Electron.*, vol. 5, no. 2, pp. 127–131, Apr. 1961.
[16] C. Elachi, *Spaceborne Radar Remote Sensing: Applications and Techniques*. New York, NY, USA: IEEE Press, 1988.
[17] M. Soumekh, *Synthetic Aperture Radar Signal Processing With MATLAB Algorithms*. Hoboken, NJ, USA: Wiley, 1999.
[18] W. M. Brown and R. J. Fredricks, "Range-Doppler imaging with motion through resolution cells," *IEEE Trans. Aerosp. Electron. Syst.*, vol. AES-5, no. 1, pp. 98–102, Jan. 1969.
[19] M. A. Richards, *Fundamentals of Radar Signal Processing*. New York, NY, USA: McGraw-Hill, 2005.
[20] I. G. Cumming and F. H. Wong, *Digital Processing of Synthetic Aperture Radar Data*. Norwood, MA, USA: Artech House, 2005.
[21] A. Ishimaru, T.-K. Chan, and Y. Kuga, "An imaging technique using confocal circular synthetic aperture radar," *IEEE Trans. Geosci. Remote Sens.*, vol. 36, no. 5, pp. 1524–1530, Sep. 1998, doi: 10.1109/36.718856.
[22] M. Pinheiro, P. Prats, R. Scheiber, M. Nannini, and A. Reigber, "Tomographic 3D reconstruction from airborne circular SAR," in *Proc. IEEE Int. Geosci. Remote Sens. Symp.*, vol. 3, Jul. 2009, pp. 21–24, doi: 10.1109/IGARSS.2009.5418239.

[23] J. Zhang, G. Liao, J. Xu, Y. Zhang, and S. Zhu, "Study on performance of bistatic circular synthetic aperture radar imaging using geometric diversity," *IET Radar, Sonar Navigat.*, vol. 12, no. 4, pp. 458–465, Apr. 2018, doi: 10.1049/iet-rsn.2017.0382.

[24] X. Zhang, Y. Zhang, Z. Zhang, and J. Jiang, "Analysis and computer simulation of circular synthetic aperture radar with single frequency," in *Proc. 7th Eur. Conf. Synth. Aperture Radar*, Jun. 2008, pp. 1–4.

[25] L. Kou, X. Wang, M. Zhu, J. Chong, and M. Xiang, "Resolution analysis of circular SAR with partial circular aperture measurements," in *Proc. Eur. Conf. Synth. Aperture Radar (EUSAR)*, 2010, pp. 665–668.

[26] V. T. Vu, T. K. Sjogren, M. I. Pettersson, and H. Hellsten, "An impulse response function for evaluation of UWB SAR imaging," *IEEE Trans. Signal Process.*, vol. 58, no. 7, pp. 3927–3932, Jul. 2010, doi: 10.1109/TSP.2010.2047503.

[27] B. Friederich, D. Damyanov, J. C. Balzer, and T. Schultze, "Reference-free material characterisation of objects based on terahertz ellipsometry," *IEEE Access*, vol. 8, pp. 186138–186147, 2020, doi: 10.1109/ACCESS.2020.3029355.

[28] T. Kubiczek and J. C. Balzer, "Material classification for terahertz images based on neural networks," *IEEE Access*, vol. 10, pp. 88667–88677, 2022, doi: 10.1109/ACCESS.2022.3200473.

**ANDREAS CZYLWIK** received the Dr.-Ing. and Habilitation degrees in optical communications from the Technical University of Darmstadt, Germany, in 1988 and 1994, respectively.

He has studied electrical engineering at the Technical University of Darmstadt, from 1978 to 1983. From 1994 to 2000, he was with the Research and Development Center (Technologiezentrum), Department of Local Area Broadband Radio Systems, Deutsche Telekom. In 2000, he became a Full Professor at the Technical University of Braunschweig, where he is heading the Research Group of Microcellular Radio Systems. Since 2002, he has been with the University of Duisburg–Essen, where he is heading the Chair of Communication Systems. His research interests include radio communications on link and system level, with special focus on adaptive multicarrier MIMO techniques. His several research activities focus on utilizing high frequency (up to THz) electromagnetic waves in applications in the field of extreme wideband communications and radar systems. He is also interested in the application of radio communications in the field of technical security systems.

Dr. Czylwik has been the Chairperson of EUSAS and the European Society for Automatic Alarm Systems, since 2014.

**DILYAN DAMYANOV** received the master's degree in communication engineering from the University of Duisburg–Essen, Germany, in 2014. From 2014 to 2021, he was a Research Assistant at the Chair of Communication Systems, University of Duisburg–Essen. From 2016 to 2021, he was a part of the "MARIE" Project for mobile material characterization and localization by electromagnetic sensing using mobile THz systems. His research interests include broadband radar sensors for fire and security applications and especially radar localization, wavefront detection, and imaging techniques.

**THORSTEN SCHULTZE** received the Diploma degree in electrical engineering from the University of Duisburg–Essen, in 2003, and the Ph.D. degree in electrical engineering, in 2010. He is currently working as an Academic Senior Councillor (Akademischer Oberrat) with the Chair of Communication Systems, University of Duisburg–Essen. His main research interests include automatic fire detection technologies and broadband microwave and THz analyses for fire and security applications.

**TOBIAS KUBICZEK** received the master's degree in communication engineering from the University of Duisburg–Essen, Germany, in 2020, where he is currently pursuing the Dr.-Ing. degree in electrical engineering. Since 2020, he has been a Research Assistant with the Chair of Communication Systems, University of Duisburg–Essen. Since 2021, he has been a part of the "MARIE" Project for mobile material characterization and localization by electromagnetic sensing using mobile THz systems. His research interests include terahertz imaging and signal processing in terms of synthetic aperture radar and material classification with the help of artificial neural networks.

**JAN C. BALZER** (Member, IEEE) received the Dipl.-Ing. (FH) degree in telecommunications from the Dortmund University of Applied Sciences, Germany, in 2008, and the Master of Science degree in electrical engineering and information technology and the Dr.-Ing. degree from Ruhr University Bochum, Bochum, Germany, in 2010 and 2014, respectively. In 2015, he joined as a Postdoctoral Fellow at the Research Group of Prof. Martin Koch, Philipp University of Marburg, Marburg, Germany. Since 2017, he has been an Assistant Professor of Terahertz Systems with the Faculty of Engineering, University of Duisburg–Essen, Germany. His research interest includes ultrafast semiconductor lasers. From ultrafast semiconductor lasers, he moved to the field of terahertz radiation generation and applications. He made contributions in the field of compact laser diode-driven THz systems, 3D-printed THz devices, high-resolution THz imaging, and THz material characterization.

**KEVIN KOLPATZECK** received the B.S., M.S., and Dr.-Ing. degrees in electrical engineering and information technology from the University of Duisburg–Essen, Germany, in 2013, 2016, and 2022, respectively.

He has investigated terahertz time-domain spectroscopy systems driven by monolithic mode-locked laser diodes, at the University of Duisburg–Essen. He is currently a Postdoctoral Researcher with the Chair of Communication Systems (NTS), University of Duisburg–Essen. His current research interests include terahertz photonics, beamforming at terahertz frequencies, and the use of terahertz technology in radar applications and non-destructive testing.